IEEE Access
Multidisciplinary | Rapid Review | Open Access Journal

Received January 27, 2020, accepted March 14, 2020, date of publication March 18, 2020, date of current version April 7, 2020.

Digital Object Identifier 10.1109/ACCESS.2020.2981596

A Novel Active Contour Model Guided by Global and Local Signed Energy-Based Pressure Force

HUAXIANG LIU[1,2], JIANGXIONG FANG[2], ZIJIAN ZHANG[3], AND YONGCHENG LIN[1]

[1]College of Mechanical and Electrical Engineering, Central South University, Changsha 410083, China
[2]School of Mechanical and Electronic Engineering, East China University of Technology, Nanchang 330013, China
[3]Department of Radiation Oncology, Central South University, Changsha 410083, China

Corresponding authors: Huaxiang Liu (felicia_liu@126.com) and Yongcheng Lin (yclin@csu.edu.cn)

This work was supported in part by the National Natural Science Foundation of China under Grant 61966001, Grant 61866001, and Grant 61463005, in part by the Natural Science Foundation of Jiangxi Province under Grant 20192BAB207028, Grant 20181BAB211017, and Grant 20171BAB202028, and in part by the Jiangxi Provincial Key Laboratory of Digital Land under Grant DLLJ201804.

ABSTRACT Active contour models (ACMs) have been widely applied in the field of image segmentation. However, it is still very challenging to construct an efficient ACM to segment images with intensity inhomogeneity. In this paper, a novel ACM guided by global and local signed energy-based pressure force (GLSEPF) is proposed. First, by computing the energy difference between the inner and outer energies of the evolution curve, a global signed energy-based pressure force (GSEPF) is designed, which can improve the robustness to initial curves. Second, a local signed energy-based pressure force (LSEPF) is introduced by computing the pixel-by-pixel energy difference within local neighborhood region, which can handle images with intensity inhomogeneity and noise. Finally, the global image information and the local energy information are used for the global and local force propagation functions, respectively. The global and local variances are used to automatically balance the weights of the GSEPF and the LSEPF, which can solve the problem of setting parameters. Meanwhile, a regularization term and a penalty term are applied to avoid the re-initialization process during iterations and smooth the level set function. Experimental results on different types of images demonstrate that the proposed model is more robust than the popular region-based and mixed ACMs for segmenting images with intensity inhomogeneity and noise. The code is available at: https://github.com/HuaxiangLiu/GLSEPF/.

INDEX TERMS Image segmentation, active contour, signed pressure force, intensity inhomogeneity.

I. INTRODUCTION

The segmentation problem is one of the important issues in computer vision applications including object extraction and tracking [1], [2]. In recent years, active contour model (ACM) has been one of the most effective segmentation algorithms, which was first proposed by Kass *et al.* [3] and extensively applied in image analysis. Its basic idea is to segment an image into non-overlapping regions with a certain similar feature by minimizing the energy function, such as intensity, color, and texture [4]. However, it is one great challenge to develop an effective image segmentation algorithm for the practice application since the real-world images usually contain noise, intensity inhomogeneity (Abbreviated as InH) caused by imaging conditions and imaging devices.

The associate editor coordinating the review of this manuscript and approving it for publication was Cristian A. Linte.

Generally speaking, according to image information used as the formulation of the energy function, the existing ACMs are classified into three categories: edge-based ACMs [3], [5], region-based ACMs [6]–[22], and the mixed ACMs [23]–[32]. The edge-based ACMs use the image gradient to construct an edge stopping function (ESP), which makes the evolution curve to move toward the object boundaries. One of the most popular edge-based ACMs is the geodesic active contour (GAC) [5]. Its basic idea is to construct an ESP to make the evolution curve stop on the exact object boundaries by incorporating image gradient and geometrically active contour into the curve evolution theory. However, the edge-based ACM is difficult to extract the desired objects from the images with weak boundaries since the gradient information is sensitive to noise and weak edges.

The region-based ACMs use the statistical region information of the inner and outer regions of the evolution curve

to formulate the energy functional, which is minimized by gradient decent method. In the region-based ACMs, every closed curve is expressed as a zero level set function (LSF) to denote a segmented region. Here, the LSF is also called signed distance function (SDF). The Chan-Vese model [6], as a representative region-based ACM, is driven by the intensity difference between the input image and the average intensities of the inside and outside regions of the evolution curve, which is based on the Mumford-Shah (M-S) model [8]. The Chan-Vese model could effectively deal with a binary phase segmentation and each segmented region was assumed as homogeneous. Compared with the edge-based ACMs, the region-based ACMs are less sensitive to initial condition and could successfully detect the object boundaries. To solve the problem of local minimum energy, a fuzzy energy-based active contour (FEAC) model [9] by incorporating the fuzzy set into the ACM [10] was proposed with strictly convex energy functional. A improved regularization term [11] was designed to avoid periodically initializing LSF. Later on, some improved FEAC-based models, such as the fuzzy region-based ACM with global and local (FRAGL) model [12] and the fuzzy level set method (FCMLSM) [13], were designed to segment different types of images. However, the region-based ACMs often result in the poor segmentation performance for images with intensity InH since they assumed that the intensities in the object and background regions are constant.

To successfully segment the images with intensity InH, Vese and Chan [7] proposed a piecewise smooth (PS) model, in which the LSF was represented by the set of discontinuity points. But its computational cost is very high. The local binary fitting (LBF) model with the region-scalable fitting energy could extract local image information, which was proposed by Li *et al.* [14], [15] with a convolutional kernel function. Its basic idea was to utilize local image information with spatially varying weight by controlling a scalable parameter to extract local image features. But, for the LBF model, four convolution operations need to be performed in each iteration, which greatly increases computational cost. More importantly, the LBF model is highly dependent on the initial positions of the evolution curves. Zhang *et al.* [16] proposed a local image fitting (LIF) model by computing the difference between the input image and the fitting intensity value. Later on, many region-based ACMs were proposed by incorporating local image information, such as the local likelihood image fitting energy model (LLIF) [17], the local hybrid image fitting energy (LHIF) model [18], the local Gaussian distribution fitting (LGDF) model [19], the weighted region-scalable fitting (WRSF) model [20], the local cosine fitting based active contour (LCFAC) model [21], the local pre-fitting based active contour (LPFAC) model [22], and the hybrid ACM with global and local information [23]. In these models, the local image information was incorporated into the energy functional and the ideal segmentation results were obtained. On the other hand, the Retinex-like image decomposition technique was used in the Chan-Vese model with bias correction (CVXB) [24] to approximate the illumination bias correction inherently. The local image information are fused into the ACM, such as the local bias field estimation [25] and the local patch similarity information [26]. However, these local region-based ACMs were sensitive to initial position, and improper initial curve led to poor segmentation results.

By taking full advantages of the edge-based and region-based ACMs, the mixed ACMs have been designed. The Geodesic-Aided Chan-Vese (GACV) model [27] consists of a GAC model and a Chan-Vese model, which combines the edge information and the region information and can selectively deal with local and global segmentation. The variational hybrid model [28] includes two fitted terms based on edges and regions, which was used to balance the average intensities of the interior and exterior regions. Li *et al.* [29] proposed a distance regularization level set evolution (DRLSE) model with a distance regularization term and a data term, which drove level set evolution toward forward-and-backward (FAB) diffusion. In the ACM with selective binary and Gaussian filtering regularized level set (SBGFRLS) proposed by Zhang *et al.* [30], a signed pressure force (SPF) function was firstly designed to construct a global ACM. The SPF as the driving force was formulated based on the difference between the input image and the average values of the inner and outer region fitting centers. Meanwhile, a Gaussian filtering function was used to regularize and smooth the LSF. Different from the ACM with SBGFRLS, an online region-based active contour model (ORACM) [31] used a simple level set function to replace the curvature approximation, and an opening and closing morphological operations to smooth the LSF. The ACM based on Hessian matrix (ACM-HM) [32] replaced the derivative of the LSF in Zhang's model [30] with the eigenvalue information of Hessian matrix, which could effectively handle with images with blurred boundaries. More ACMs were found in the literature [33]–[35] by incorporating different image information into the SPF, such as the global image information model (GSRPF) [33], the local signed pressure force (LSPF) model [34], the SPF-LIF model [35], the global and local weighted signed pressure force (GL-SPF) model [36], and weighted hybrid region-based signed pressure force (WHRSPF) [37]. However, the SPFs in these models utilized the global image information and could not extract desired objects from images with intensity InH.

In this paper, a novel ACM guided by the global and local signed energy-based pressure force, which is called GLSEPF, is proposed to segment images with intensity InH. Our main contributions can be summarized as:

(1) By computing the energy difference between the inner and outer energies of the evolution curve, a novel ACM driven by a global signed energy-based pressure force (LSEPF) as the driving force is designed to deal with complex images. What's more, a force propagation function (FPF) in the global data term is introduced, which can automatically be tuned in terms of image feature during iterations.

(2) To extract the exact object boundaries for images with intensity InH and noise, a local signed energy-based pressure force (LSEPF) is designed by computing the pixel-by-pixel energy difference within the local neighborhood region. Meanwhile, its corresponding FPF in the local data term is introduced, which can eliminate the problem of setting parameter.

(3) In the implementation process, the global and local variances is applied to automatically balance the weights of the GSEPF and the LSEPF. In addition, a regularization term and a penalty term are added to avoid the re-initialization process and smooth the LSF during iterations.

The rest of this paper is arranged as follows. The related works are reviewed in Section 2. Section 3 describes the proposed model, including the formulation of the GSEPF and LSEPF functions, the level set formulation, and the description of the algorithm steps. Section 4 shows experimental results compared with the popular ACMs. Finally Section 5 concludes this paper.

II. RELATED WORKS

Chan and Vese [6] designed a region-based ACM, which is a special example of the Mumford-Shah model [9]. Let $I(x) : \Omega \to R^+$ be an input image with point x, and $C : [0, \quad 1] \to \Omega$ be a close contour, which divides the image domain into the internal region C_{in} and the external region C_{out}. The Chan-Vese model is written as:

$$E^{CV}(C, c_1, c_2) = \lambda_1 \int_{C_{in}} |I(x) - c_1|^2 \, dx + \lambda_2 \int_{C_{out}} |I(x) - c_2|^2 \, dx + \mu \cdot length(C) \quad (1)$$

where λ_1, λ_2 and μ are three positive constants, c_1 and c_2 are two piecewise constants which denote the average intensities of the internal region C_{in} and the external region C_{out}, respectively.

In the level set method, the closed curve $\boldsymbol{C}$ is presented as the zero level set of a Lipschitz function $\phi(x)$.

$$\begin{cases} \phi(x) > 0 & \text{if}(x) \in \text{Inside}(C) \\ \phi(x) = 0 & \text{if}(x) \in \text{On}(C) \\ \phi(x) < 0 & \text{if}(x) \in \text{Outside}(C) \end{cases} \quad (2)$$

To minimize the energy functional by replacing the curve C with the LSF, the Chan-Vese model can be rewritten as:

$$E^{CV}(c_1, c_2, \phi) = \mu \cdot \int_\Omega \delta(\phi) \, |\nabla \phi| \, dx + \lambda_1 \int_\Omega (I(x) - c_1)^2 H(\phi) dx + \lambda_2 \int_\Omega (I(x) - c_2)^2 (1 - H(\phi)) dx \quad (3)$$

where $H(x)$ and $\delta(x)$ denote the Heaviside function and the Dirac delta function, respectively, and can be defined as:

$$H(x) = \begin{cases} 1 \text{ if} x > 0 \\ 0 \text{ if} x < 0 \end{cases}, \quad \delta(x) = \frac{d}{dx} H(x) \quad (4)$$

Then, the gradient descent method is used to solve the minimization problem in (3). With artificial time t, the updated level set formulation is written as:

$$\frac{\partial \phi}{\partial t} = \delta(\phi) \left(\mu div(\frac{\nabla \phi}{|\nabla \phi|}) - \lambda_1 (I(x) - c_1)^2 + \lambda_1 \, (I(x) - c_2)^2 \right) \quad (5)$$

here c_1 and c_2 are equal to

$$c_1 = \frac{\int_\Omega H(\phi) I(x) dx}{\int_\Omega H(\phi) dx}, \quad c_2 = \frac{\int_\Omega [1 - H(\phi)] I(x) dx}{\int_\Omega (1 - H(\phi)) dx} \quad (6)$$

Later on, to take the advantages of the GAC model and the Chan-Vese model, the mixed ACMs [26] driven by the SPF were proposed, simplified as the Zhang's model [26]. The SPF function was constructed based on the intensity difference between the input image and the average intensities of the inner and outer regions of the evolution curve, which can efficiently segment homogeneous images. The SPF function is defined as:

$$spf(I((x)) = \frac{I(x) - \frac{c_1 + c_2}{2}}{\max\left(\left|I(x) - \frac{c_1 + c_2}{2}\right|\right)} \quad (7)$$

where two constants c_1 and c_2 are the average intensities of the regions inside and outside the curve C, respectively.

The edge stopping function (ESF) in the GAC model is replaced with the SPF function. The evolving equation is written as follows:

$$\frac{\partial \phi}{\partial t} = spf(I(x)) \left(div(\frac{\nabla \phi}{|\nabla \phi|}) + \alpha \right) |\nabla \phi| + \nabla spf(I(x)) \cdot \nabla \phi \quad (8)$$

where α is a parameter of the speed to control the LSF updating, and $\nabla \phi$ is the gradient of the LSF.

To avoid the re-initialization process of the LSF at each iteration, a Gaussian filter is used to regularize the binary LSF. So the evolution equation (8) by ignoring the curvature-based term, which is used to regularize the LSF, is written as:

$$\frac{\partial \phi}{\partial t} = spf(I(x)) \cdot \alpha \, |\nabla \phi| \quad (9)$$

To eliminate the parameter α in (9) and shorten the time to detect the object boundaries, an efficient level function is set to update the formulation [30], and its evolution equation is written as:

$$\frac{\partial \phi}{\partial x} = H \, (spf \, (I(x))) \cdot \phi(x) \quad (10)$$

where $spf \, (\cdot)$ is the SPF function defined in (7). Different from the Zhang's model, a binary level set formula can express the internal and external regions using different signs, and the morphological opening and closing operations can regularize the LSF.

The ACM with a global weighted SPF (GWSPF) and a local weighted SPF (LWSPF) [36] is given as:

$$spf_{HR}(I(x)) = w_g \cdot \frac{I(x) - (d_{NG1} c_1 + d_{NG2} c_2)}{\max(|I(x) - (d_{NG1} c_1 + d_{NG2} c_2)|)} + w_l \cdot \frac{I(x) - (d_{NL1} f_1 + d_{NL2} f_2)}{\max(|I(x) - (d_{NL1} f_1 + d_{NL2} f_2)|)} \quad (11)$$

where w_g and w_l are two weighted variables. d_{NG1} and d_{NG2}, d_{NL1} and d_{NL2} are two pairs of the global and local minimum absolute differences of pixel intensities of the inner and outer regions, respectively. c_1 and c_2 are two average intensities of the internal region C_{in} and the external region C_{out} defined in (2), respectively. f_1 and f_2 are the mean values of the inner and outer regions, i.e.,

$$\begin{cases} f_1 = mean(I(x) \in (x \in \Omega | (\phi(x) > 0)) \cap W_g(x)) \\ f_2 = mean(I(x) \in (x \in \Omega | (\phi(x) < 0)) \cap W_g(x)) \end{cases} \tag{12}$$

where $W_g(x)$ is the local window function with the local parameter g.

It is obvious that the SPF function is constructed based on the difference between the input image and the fitted intensity of the inner and outer regions of the evolution curve. In these models, the intensities of the inner and outer regions of the evolution curve in given image are assumed as homogeneous. Therefore, it is difficult to accurately extract the desired objects from images with intensity InH.

III. PROPOSED MODEL

From the above analysis, the ACMs driven by the SPF take advantages of the edge-based and region-based ACMs, and can obtain satisfactory segmentation results for homogeneous images. In these models, the SPF function is constructed based on the global image information, which can not extract local image features. In fact, the real-world images mainly exist in intensity InH. Thereby, it is difficult to apply these models into the practice. In addition, the updating speed α in the Zhang's model is difficult to appropriately set. To solve these problems, a novel ACM guided by the GLSEPF is proposed. In this section, the formulation of the GSEPF and LSEPF, the level set formulation, and the implementation process are presented in details.

A. FORMULATION OF THE GSEPF

Let $I(x) \in R^d$ be a given vector value image with point x in the image domain Ω, where $d = 1$ for the gray image while $d = 3$ for the color image. The evolution curve partitions the image domain Ω into two regions: the internal region C_{in} and the external region C_{out}. In Fig. 1, the yellow line denotes the evolution curve. Two corresponding variables are defined as:

$$\begin{cases} c_1 = mean(I(x) \in \{x \in \Omega | \phi(x) > 0\}) \\ c_2 = mean(I(x) \in \{x \in \Omega | \phi(x) < 0\}) \end{cases} \tag{13}$$

where $I(x)$ is the input image of the pixel location x in the image domain Ω. In fact, the constants c_1 and c_2 are average intensities of the internal region C_{in} and the external region C_{out}, respectively.

The internal and external energies of the evolution curve $e_1(x)$ and $e_2(x)$ in the image domain Ω can be defined as:

$$\begin{cases} E_1^g(I(x)) = \int_\Omega (I(x) - c_1)^2 \, dx \\ E_2^g(I(x)) = \int_\Omega (I(x) - c_2)^2 \, dx \end{cases} \tag{14}$$

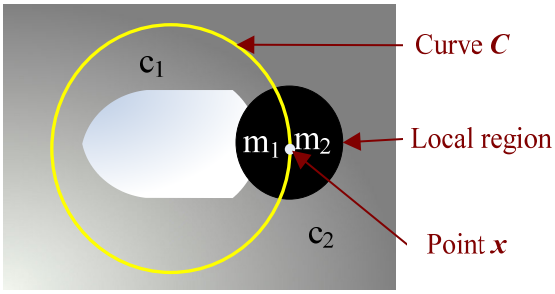

FIGURE 1. The description of the evolution curve (Yellow line). The local region is formulated centered at point x on the evolution curve C.

On the basis of the above energy functions (14), the global sign energy-based pressure force (GSEPF) function is defined as:

$$\begin{aligned} spf_{GE}(I((x)) &= \frac{E_2^g(I(x)) - E_1^g(I(x))}{\max\left(\left|E_2^g(I(x)) - E_1^g(I(x))\right|\right)} \\ &= \frac{\int_\Omega (I(x)-c_2)^2 \, dx - \int_\Omega (I(x)-c_1)^2 \, dx}{\max\left(\left|\int_\Omega (I(x)-c_2)^2 \, dx - \int_\Omega (I(x)-c_1)^2 dx\right|\right)} \end{aligned} \tag{15}$$

From (15), it is intuitive that the GSEPF function is similar to the SPF function in the Zhang's model [30], and it can extract the global image characteristics by incorporating the global image information. The direction of motion of the evolution curve is analyzed as follows. Suppose the average intensities of the foreground and background regions are c_o and c_b ($c_o > c_b$), the moving direction of the evolution curve depends on the following equation:

$$\begin{aligned} \Delta E^g(I(x)) &= E_2^g(I(x)) - E_1^g(I(x)) \\ &= \int_\Omega (c_2 - c_1) \left(I(x) - \frac{c_1 + c_2}{2} \right) dx \end{aligned} \tag{16}$$

Since the average intensity of the foreground region is not equal to that of the background region, the moving direction of the evolution curve is dependent on the equation $I(x) - \frac{c_1+c_2}{2}$. In Fig. 2(a), the evolution curve C completely contains the object region, the average intensity of the inner region is smaller than that of the foreground region, and the average intensity of the outer region is nearly equal to that of the background region, namely, $c_o > c_1$ and $c_2 \approx c_b$. Thus, $c_b < (c_1 + c_2)/2 < (c_b + c_o)/2 < c_o$. The evolution curve will shrink toward the object region. Contrarily, the evolution curve is inside the object region shown in Fig. 2(b), the average intensity of the outer region is larger than that of the background region, and the average intensity of the inner region is nearly equal to that of the foreground region, namely $c_b < c_2$ and $c_1 \approx c_o$. Hence, there is $c_o > (c_1 + c_2)/2 > (c_b + c_o)/2 > c_b$, which drives the curve to expand toward the objects. In Fig. 2(c), the average intensity difference of the inner region is larger than that of the outer region, which is similar to Fig. 2(a). In Fig. 2(d), the average intensity difference of the outer region is larger than that of the inner

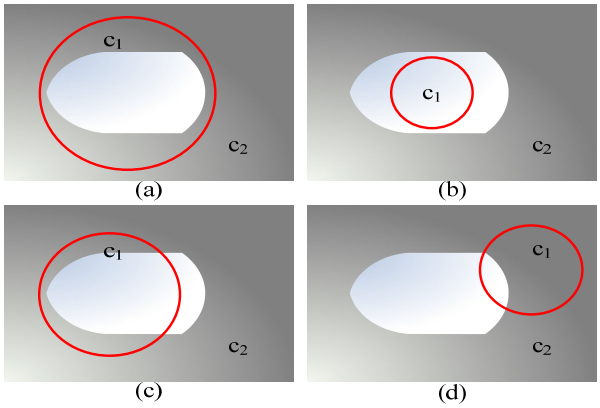

FIGURE 2. Different locations of the evolution curve (Red line). (a) The evolution curve is outside the object region; (b)The evolution curve is inside the object region; (c-d) The evolution curve intersects the object region.

region, which is similar to Fig. 2(b). In the same way, the same conclusion can be obtained when the average intensity of the foreground region is smaller than that of the background region ($c_b < c_o$).

B. FORMULATION OF THE LSEPF

In the local region (the black circle shown in Fig. 1), let x be a point on the evolution curve C, point y be independent of spatial variable x, and the local region Ω_x centered at x with the radius r can be represented as $\Omega_x = \{|y-x| \le r \ \ y \in \Omega\}$. The local region Ω_x includes the inner region $\Omega_1 = \{|y-x| \le r \ \ y \in (\Omega \cap \phi(y) > 0)\}$ and the outer region $\Omega_2 = \{|y-x| \le r \ \ y \in (\Omega \cap \phi(y) < 0)\}$, respectively. The evolution curve C divides the black circle in Fig. 1 into two regions corresponding to the inner and outer regions of the evolution curve. Two average intensities m_1 and m_2 in the local region Ω_x are respectively defined as follows:

$$\begin{cases} m_1 = mean(y \in \Omega_1, \quad \Omega_1 = ((\Omega_x \cap (\phi(y) > 0))) \\ m_2 = mean(y \in \Omega_2, \quad \Omega_2 = ((\Omega_x \cap (\phi(y) < 0))) \end{cases} \tag{17}$$

where the constants m_1 and m_2 are the average intensities of the inner and outer regions in the image domain Ω_x, respectively.

For point x, the internal and external energies of the evolution curve $e_1^l(x)$ and $e_2^l(x)$ in the local region Ω_x are respectively written as:

$$e_1^l(x) = \int_{\Omega_1} (I(y) - m_1)^2 \, dy, e_2^l(x) = \int_{\Omega_2} (I(y) - m_2)^2 \, dy \tag{18}$$

The Gaussian kernel function [12] is often used to extract the local image information. Thus, two local energies $e_1^l(x)$ and $e_2^l(x)$ can be replaced as follows:

$$\begin{cases} e_1^l(x) = \int_{\Omega_x} \kappa_\sigma(x-y) \, (I(y) - m_1)^2 \, H(y) dy \\ e_2^l(x) = \int_{\Omega_x} \kappa_\sigma(x-y) \, (I(y) - m_2)^2 \, (1 - H(y)) dy \end{cases} \tag{19}$$

where $\kappa_\sigma(\cdot)$ is Gaussian kernel with a scale parameter σ.

Correspondingly, two local energy functions $E_1^l(x)$ and $E_2^l(x)$ in the image domain Ω can be written as follows:

$$\begin{cases} E_1^l(I(x)) = \int_\Omega e_1^l(x) dx \\ \qquad = \int_\Omega \int_{\Omega_x} \kappa_\sigma(x-y) \, (I(y) - m_1)^2 \, H(x) dy dx \\ E_2^l(I(x)) = \int_\Omega e_2^l(x) dx \\ \qquad = \int_\Omega \int_{\Omega_x} \kappa_\sigma(x-y) \, (I(y) - m_2)^2 \, (1 - H(x)) dy dx \end{cases} \tag{20}$$

By combining two local energies in (20), the LSEPF is defined as:

$$\begin{aligned} & spf_{LE}(I((x)) \\ &= \frac{E_2^l(I(x)) - E_1^l(I(x))}{\max\left(\left|E_2^l(x) - E_1^l(x)\right|\right)} \\ &= \frac{\int_\Omega (I(x) - c_2)^2 \, (1 - H(x)) dx - \int_\Omega (I(x) - c_1)^2 \, H(x) dx}{\max\left(\left|\int_\Omega \left((I(x) - c_2)^2 \, (1 - H(x)) - (I(x) - c_1)^2 \, (H(x))\right) dx\right|\right)} \end{aligned} \tag{21}$$

In the following section, the moving direction of evolution curve will be explained. Suppose that the average intensities of the local foreground and background regions are c_o and c_b ($c_o > c_b$), respectively. For point x, the moving direction for point x on the evolution curve is dependent on the difference between the local energies $e_1^l(x)$ and $e_2^l(x)$. Similar to the energy difference in the GSEPF, the local energy difference between the energies $e_1(x)$ and $e_2(x)$ is rewritten as:

$$\begin{aligned} \Delta e^l(x) &= \Delta e_2(x) - \Delta e_1(x) \\ &= \int_{\Omega_x} (\kappa_\sigma(x-y) \, (I(y) - m_2)^2 - \kappa_\sigma(x-y) \, (I(y) - m_1)^2) dx \\ &= 2 \int_{\Omega_x} \kappa_\sigma(x-y) (I(y) - \frac{m_1 + m_2}{2})(m_1 - m_2) \end{aligned} \tag{22}$$

In (13), since the average intensities m_1 and m_2 are not equal ($m_1 > m_2$), the direction of the driving force for point x depends on the term $I(y) - \frac{m_1+m_2}{2}$, which is the intensity difference between the input intensity and the average intensities of the inside and outside regions. For point x inside the object region in Fig. 3(a), the average intensity in the inner region ($m_1 \approx c_o$) is close to that of the foreground region, and the average intensity of the outer region ($m_2 > c_b$) is larger than that of the background region. So, $c_b < (c_o + c_b)/2 < (m_1 + m_2)/2 < c_o$, which drives the evolving curve to move toward the background region. On the contrary, for point x outside the object region (Fig. 3b), the intensity average of the outer region ($m_2 \approx c_b$) is close to that of the background region, and the average intensity of the inner region ($m_1 < c_0$) is smaller than that of the foreground region. So, $c_b < (m_1 + m_2)/2 < (c_o + c_b)/2 < c_o$, i.e., the evolution curve will move toward the object region. For point x on the object boundary (Fig. 3c), the average intensity of the outer regions in the evolution curve is $(c_o + c_b)/2 \approx (m_1 + m_2)/2$ when the contour reaches the exact boundary. For the same reason, the direction of motion for point x is consistent with the above discussion when the average intensity of the local foreground region ($c_o < c_b$) is smaller than that of the local background region.

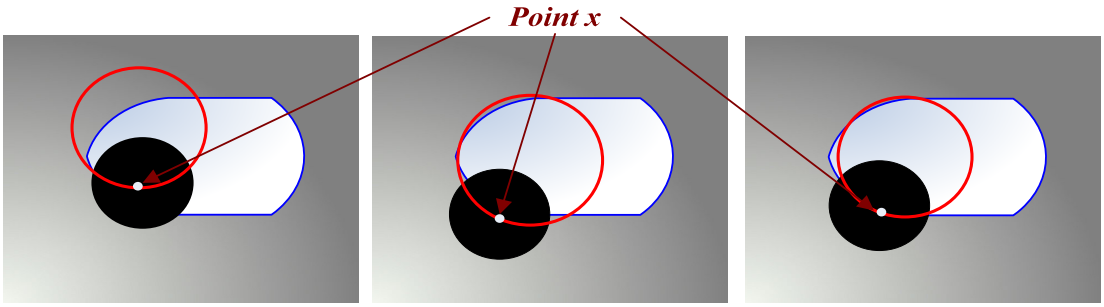

FIGURE 3. Different locations of the evolution curve (Red line). (a): The evolution curve is outside the object region; (b)The evolution curve is inside the object region; (c-d) The evolution curve intersects the object region.

C. LEVEL SET FORMULATION

To maintain the smoothness of the evolution curve and avoid the re-initialization process at each iteration, a regularization term and a penalty term are fused into the model. Following the SPF formulation in the Zhang's model [30], the level set formulation of the proposed model is defined (23) as shown at the bottom of the next page, where μ and ν are two constants, w_g and w_l are two weighted variables, which is used to balance the effects of the GSEPF and LSEPF functions. In (23), the first and second terms denote the global data and the local data, respectively. The third term is the regularization, and the last term is penalty term.

Unlike the Zhang's model with a fixed force α, two adaptive force propagation functions are used to control the global and local force of the inner and outer regions of the curve. Two force propagation function are defined as:

$$\begin{cases} \alpha_1\left(I(x)\right) = |c_1 - c_2| \\ \alpha_2\left(I(x)\right) = \max\left(\left|E_2^l(x) - E_1^l(x)\right|\right) \end{cases} \tag{24}$$

Therefore, the evolution equation in (23) is rewritten as:

$$\begin{aligned} \frac{\partial \phi}{\partial t} &= w_g \cdot spf_{GE}(I(x)) \cdot |c_1 - c_2| \cdot \nabla\phi \\ &\quad + w_l \cdot spf_{LE}(I(x)) \cdot \alpha_2(I(x)) \cdot \nabla\phi \\ &\quad + \mu\delta(\phi) \cdot div\left(\frac{\nabla\phi}{|\nabla\phi|}\right) + \nu\left(\nabla^2\phi - div(\frac{\nabla\phi}{|\nabla\phi|})\right) \\ &= w_g \cdot \frac{\Delta E^g(I(x))}{\max\left(|\Delta E^g(I(x))|\right)} \cdot |c_1 - c_2| \cdot \nabla\phi \\ &\quad + w_l \cdot \frac{E_2^l(I(x)) - E_1^l(I(x))}{\max\left(\left|E_2^l(I(x)) - E_1^l(I(x))\right|\right)} \\ &\quad \times \max\left(\left|E_2^l(I(x)) - E_1^l(I(x))\right|\right) \cdot \nabla\phi \\ &\quad + \mu\delta(\phi) \cdot div\left(\frac{\nabla\phi}{|\nabla\phi|}\right) + \nu\left(\nabla^2\phi - div(\frac{\nabla\phi}{|\nabla\phi|})\right) + \\ &= w_g \cdot \frac{\Delta E^g(I(x))}{\max\left(|\Delta E^g(I(x))|\right)} \cdot |c_1 - c_2| \cdot \nabla\phi \\ &\quad + w_l \cdot \left(E_2^l(I(x)) - E_1^l(I(x))\right) \cdot \nabla\phi \\ &\quad + \mu\delta(\phi) \cdot div\left(\frac{\nabla\phi}{|\nabla\phi|}\right) + \nu\left(\nabla^2\phi - div(\frac{\nabla\phi}{|\nabla\phi|})\right) \end{aligned} \tag{25}$$

where the difference of the global energy $\Delta E^g(I(x))$ is defined as

$$\Delta E^g(I(x)) = E_2^g(I(x)) - E_1^g(I(x)) \tag{26}$$

Two weighted variables are defined as:

$$w_g = \frac{\sigma_g^2}{\sigma_g^2 + \sigma_l^2}, w_l = \frac{\sigma_l^2}{\sigma_g^2 + \sigma_l^2} \tag{27}$$

where σ_g and σ_l are the global and local variances in the given image, respectively, which are defined as:

$$\begin{cases} \sigma_g^2 = \int_\Omega \left(I(x) - m_g\right)^2 dx \; m_g = mean(I(x)) \\ \sigma_l^2 = \int_\Omega \int_{\Omega_x} \left(I(x) - m_l\right)^2 dx \; m_l = \frac{\int_{\Omega_x} I(x) dx}{N_l} \end{cases} \tag{28}$$

where N_l is the pixel number in the local image domain Ω_x.

In (25), it can be seen that the force propagation function $\alpha_1(I(x)) = |c_1 - c_2|$ in the global data term can automatically balance the interior and exterior forces of the curves using the global image information. The propagation force increases when the evolving curve are not in the vicinity of the boundaries while the force decreases when the curve is close to the boundaries. The force propagation function in the local data term simplifies the computational cost of the LESPF. Therefore, the advantage is that the proposed model can avoid the problem of setting fixed parameters.

D. DESCRIPTION OF ALGORITHM STEPS

The procedure of implementation is summarized as:

1. Specify a given image, and initial parameters: the maximum number of iterations, two constants μ and ν, the local window size k and standard deviation σ in (19).

2. Initialize the LSF

$$\phi(x) = \begin{cases} \rho & x \in \Omega_b \\ -\rho & x \in \Omega - \Omega_b \end{cases} \tag{29}$$

where ρ is a positive constant, and Ω_b is a subset of the image domain Ω.

3. Compute two weighted variables w_g and w_l by combining (27) and (28).

4. Compute the variables: two global average intensities c_1 and c_2 using (13), and two local average intensities m_1 and m_2 using (17). Then, according to intensity InH, judge whether

the average intensity of the object region is larger or smaller than that of the background region or not.

5. Compute the global and local energy functions: $E_1^g(I(x))$, $E_2^g(I(x))$, $E_1^l(I(x))$ and $E_2^l(I(x))$ by combining (14), (18), and (20).

6. Update the level set function in (25) by combing the force propagation function (24).

7. Repeat steps 4-6 till the iterations are finished.

IV. EXPERIMENTS AND RESULTS

In this section, the segmentation performance of the proposed model on the images with intensity InH and noise are validated. The following experiments are implemented on a 3.2-GHz Intel 4-core PC computer with 3 GB of memory using the Matlab programming language. If not specified, the fixed parameters are set as: $\nu = 1$, $\mu = 0.001 \times 255^2$, and the iteration number Num=100.

To fairly compare the proposed model with the popular ACMs, the Dice coefficient [37] is used to quantitatively evaluate the accuracy of the proposed model. The Dice coefficient between two regions is defined as follows:

$$Dic(A, B) = \frac{2\,(A \cap B)}{A + B} \tag{30}$$

where A and B denote the given baseline object region and the object region, respectively. It is obvious that the closer the Dice coefficient value is to 1, the better the segmentation results we obtain.

A. SEGMENTATION RESULTS ON SYNTHETIC IMAGES

Fig. 4 shows the segmentation results on a synthetic image with severe intensity InH. The local widow sizes are all set to 5. The original image with red initial curve is shown in Fig. 4(a). The intermediate stopping positions of the evolution curves during 5th, 10th, 15th, and 20th iterations are shown in Figs. 4(b)-(e), respectively. To further verify the robustness of the proposed model, the segmentation results on the synthetic image by adding different types of noise are shown in Fig. 5. Three images in the 1st column are from the clean image corrupted by the speckle noise with the mean 0 and the variance 0.01, the Gaussian noise with the mean 0 and the variance 15, and the salt and pepper noise with densities of 0.05, respectively. From the 2nd column to the 4th column, the intermediate stopping positions of the evolving curves during 5th, 10th, and 15th iterations are shown, respectively. The last column shows the final stopping positions of the evolution curves. It can be seen that the proposed model

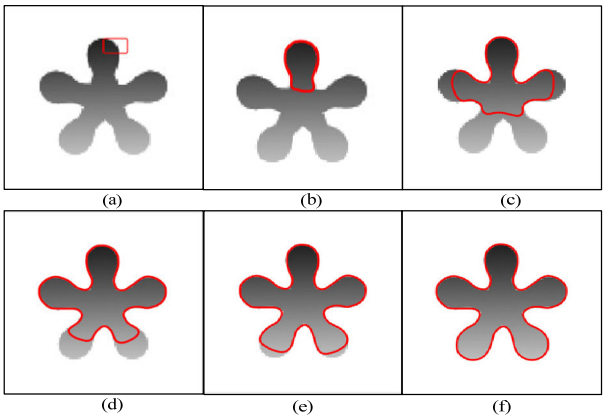

FIGURE 4. The segmentation results of the proposed model. (a) The original image with initial curve.; (b)-(e) The intermediate stopping positions of the evolution curve during 5th, 10th, 15th, and 20th iterations; (f) The final stopping position of the evolution curve.

can still extract these objects from these noisy images though the images is gravely corrupted by different types of noise. So, it can be concluded that the proposed model is robust to noise.

In this section, the tested experiments are used to validate that the proposed model is robust to initial curves. Fig. 6 shows the segmentation results of the proposed model with different initial shapes for inhomogeneious images. The initial contours with different shapes and positions are shown in the 1st row, and the final stopping positions of the curves are shown in the 2nd row, respectively. The results shows the proposed model with different initial conditions (shapes and positions) can obtain similar results. In conclusion, our model is robust to initialization.

B. SEGMENTATION RESULTS ON NATURAL IMAGES

In fact, the real-world images are often in the presence of intensity inhomogeneity. In the following experiments, the natural images from Berkeley Image Dataset [38] with serious intensity inhomogeneity are performed using the proposed method. The segmentation results are shown in Fig. 7. It is intuitive that our model can accurately extract the desired objects.

C. EFFECTS OF THE GSEPF AND THE LSEPF

The following experiments will test the effects of the global and local data terms driven by the GSEPF and LSEPF, respectively. In this work, the ACM with the signed global energy-based pressure force is called as the GSEPF model,

$$\frac{\partial \phi}{\partial t} = \overbrace{\overbrace{w_g \cdot spf_{GE}(I(x)) \cdot \alpha_1(I(x)) \cdot \nabla\phi}^{Global\ Data\ Term} + \overbrace{w_l \cdot spf_{LE}(I(x)) \cdot \alpha_2(I(x)) \cdot \nabla\phi}^{Local\ Data\ Term}}^{Data\ Term} + \underbrace{\mu\delta(\phi) \cdot div\left(\frac{\nabla\phi}{|\nabla\phi|}\right)}_{Regularization\ Term} + \underbrace{\nu\left(\nabla^2\phi - div(\frac{\nabla\phi}{|\nabla\phi|})\right)}_{Penety\ Term} \tag{23}$$

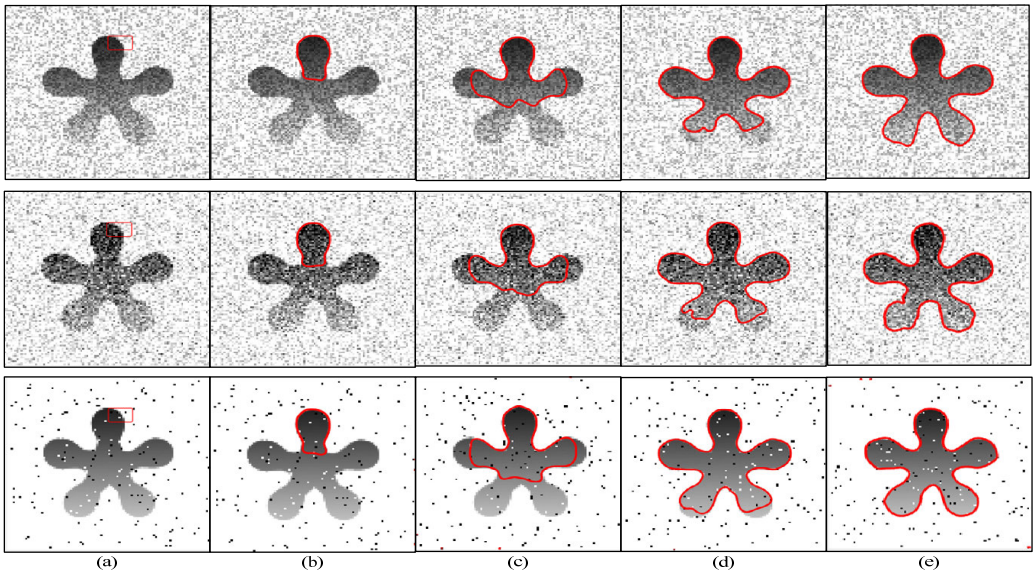

FIGURE 5. Segmentation results on the synthetic image by adding different types of noise. In the 1st column: noisy images with initial contours; From the 2nd column to 4th column: the stopping positions of the curves during 5th, 10th, and 15th iterations, respectively; The 5th column: the finial stopping positions of the curves.

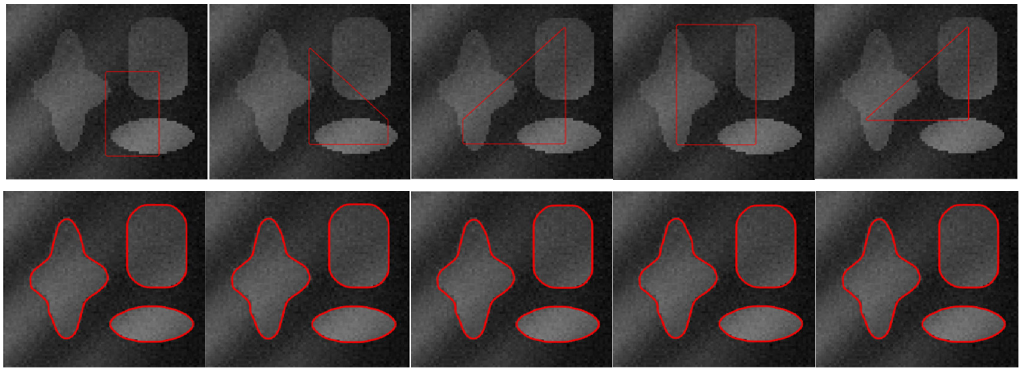

FIGURE 6. Segmentation results for inhomogeneious image with different initial curves. In the 1st row: initial contours with different shapes and positions; The 2nd row: the finial stopping positions.

and the ACM with the signed local energy-based pressure force is called as the LSEPF model. The level set formulation of the GSEPF and LSEPF models are written as:

$$\text{GSEPF model: } \frac{\partial \phi}{\partial t} = \frac{\Delta E^g(I(x))}{\max\left(|\Delta E^g(I(x))|\right)} \cdot |c_1 - c_2| \cdot \nabla\phi + \mu\delta(\phi) \cdot div\left(\frac{\nabla\phi}{|\nabla\phi|}\right) + \nu\left(\nabla^2\phi - div(\frac{\nabla\phi}{|\nabla\phi|})\right) \tag{31}$$

$$\text{LSEPF model: } \frac{\partial \phi}{\partial t} = \left(E_2^l(I(x)) - E_1^l(I(x))\right) \cdot \nabla\phi + \mu\delta(\phi) \cdot div\left(\frac{\nabla\phi}{|\nabla\phi|}\right) + \nu\left(\nabla^2\phi - div(\frac{\nabla\phi}{|\nabla\phi|})\right) \tag{32}$$

Fig. 8 demonstrates the segmentation results on the cardiac and remote sensing images using the GSEPF model, the LSEPF model and the GLSEPF model, respectively. Three models with the same initial curves are shown in the 1st column. The finial stopping positions of the evolution curves corresponding to the GSEPF model, the LSEPF model, and the GLSEPF model are shown from the 2nd column to the 4th column, respectively. From Fig. 8, it can be seen that the GESPF model can extract more detailed information than the LSEPF models while the LSEPF model can extract more local image features than the GESPF model. The GESPF with the global image information is robust to initial curve while the LSEPF model is robust to noise. By incorporating the GSEPF and the LSEPF model, the proposed model can accurately detect object boundaries.

D. COMPARISIONS OF THE PROPOSED MODEL WITH THE POPULAR ACMS

Figs. 9-15 show the segmentation results on the medical images with intensity InH compared with thirteen popular ACMs including the C-V model [6], the LBF model [14],

FIGURE 7. Segmentation results on Berkeley Image Dataset. The 1st row: the input image with initial contours; The 2nd row: the finial stopping positions.

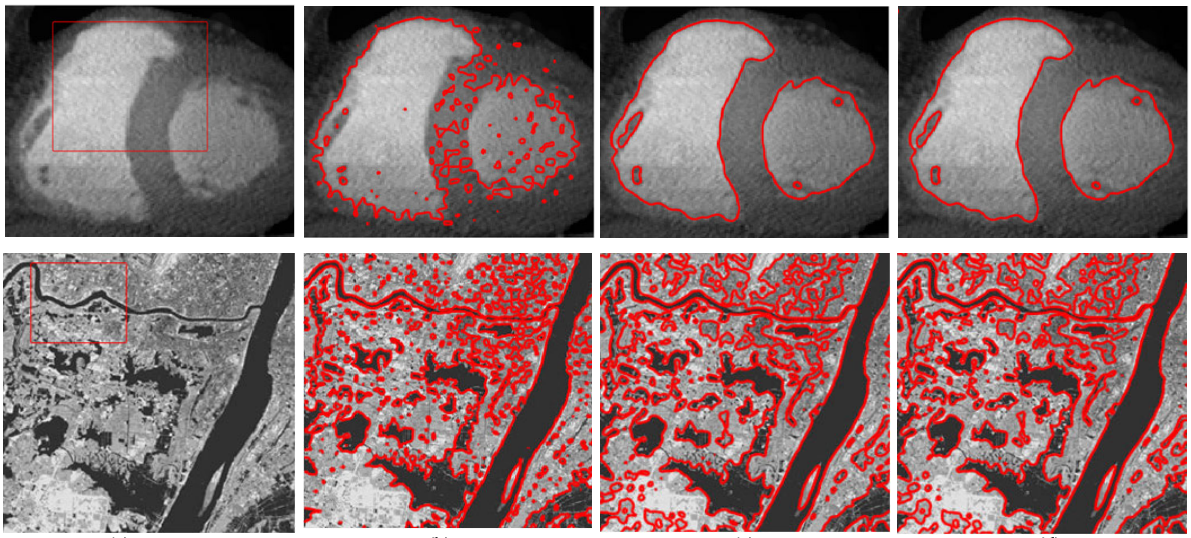

FIGURE 8. Segmentation results using the GESPF model, the LESPF model, and the GLESPF model, respectively. The 1st column: the input image with initial contours; From the 2nd column to the 4th column: the finial stopping positions corresponding to the GRSPF model, the LRSPF model, and the proposed model, respectively.

the LIF model [16], the LGDF model [19], the LPFAC model [22], the CVXB model [24], the Zhang's model [30], the ORACM model [31] without morphological operation (ORACM-WT), the ORACM model with morphological operation (ORACM-WH), the ACM-HM model [32], the GSRPF model [33], the WHRSPF model [37], and the FRAGL model [12]. For these severely inhomogeneious images, accurately extracting the desired objects is a challenging task. In the proposed model, the local window sizes are set to 5, 5, 5, 5, 7, 12, and 12, respectively. In Figs. 10-15, each (a) shows the original images with initial curves. In Figs. 9-15, fourteen segmentation results are shown using the C-V model, the LBF model, the LIF model, the LGDF model, the LPFAC model, the CVXB model, the Zhang's model, the ORACM-WT model, the ORACM-WH model, the ACM-HM model, the GSRPF model, the WHRSPF model, the FRGAL model, and the proposed model, respectively.

From Figs. 9-15, it is intuitive that the C-V model and the Zhang's model have too many small regions since they are based on the global image information and assume that the object region is homogeneous. The local region-based ACMs, such as the LBF model, the LIF model, the LGDF model, and the CVXB model, cannot accurately exact the desired objects since the local minimum energy causes the segmentation results sensitive to initial curves. The FRAGL model and the ORACM-WH model have better results than the ORACM-WT model, the GRSPF model, and the ACM-HM model. As seen from these figures, it is intuitive that only the proposed model by incorporating global and local image information can extract desired objects from these images with severely intensity InH. To quantitatively present the segmentation performance, Fig. 16 lists the comparative results in terms of the Dice coefficient.

The segmentation results are analyzed as follows. The C-V model is constructed based on the global image feature, which

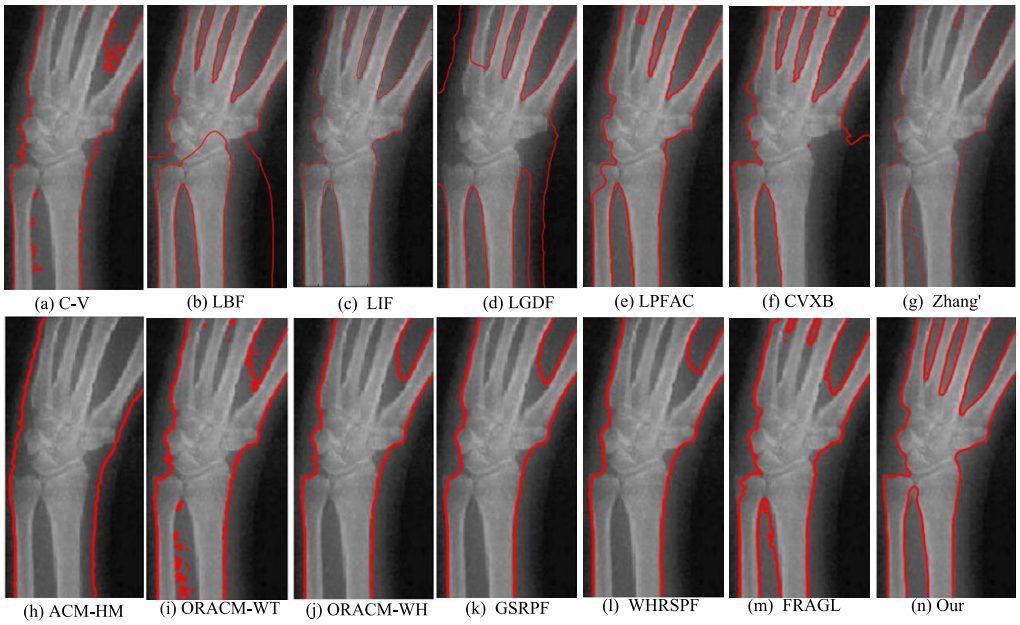

FIGURE 9. Segmentation results of the medical image using fourteen models. (a) The input image with Initial curve; (b) C-V; (c) LBF; (d) LIF; (e) LGDF; (f) LPFAC; (g) CVXB; (h) Zhang's; (i) ACM-HM; (j) ORACM-WT; (k) ORACM-WH; (l) GSRPF; (m) WHRSPF; (n) FRAGL; (o) our model.

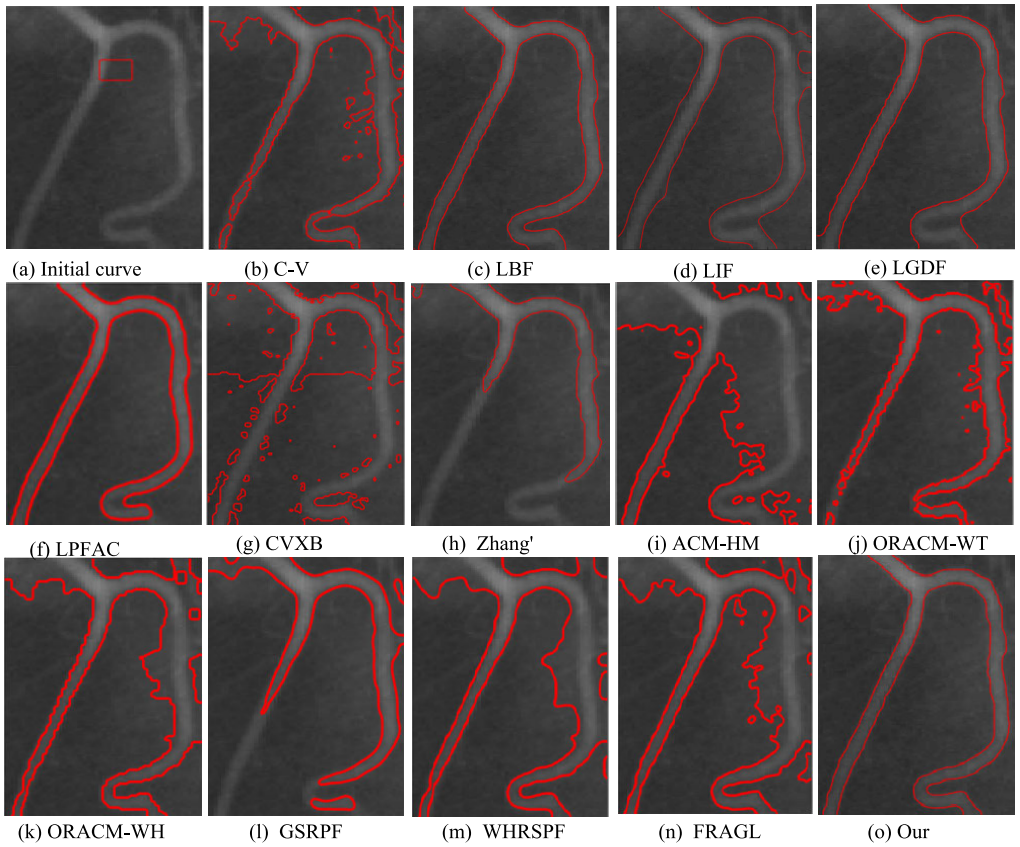

FIGURE 10. Segmentation results of the medical image using fourteen models. (a) The input image with Initial curve; (b) C-V; (c) LBF; (d) LIF; (e) LGDF; (f) LPFAC; (g) CVXB; (h) Zhang's; (i) ACM-HM; (j) ORACM-WT; (k) ORACM-WH; (l) GSRPF; (m) WHRSPF; (n) FRAGL; (o) our model.

cannot deal with intensity InH. The LBF model with local image information can deal with intensity InH in some extent. But its segmentation results are dependent on initial curve. The LIF model takes advantage of the means and variances in local regions to construct the local image fitting energy. But it is difficult to set the suitable size of the local window.

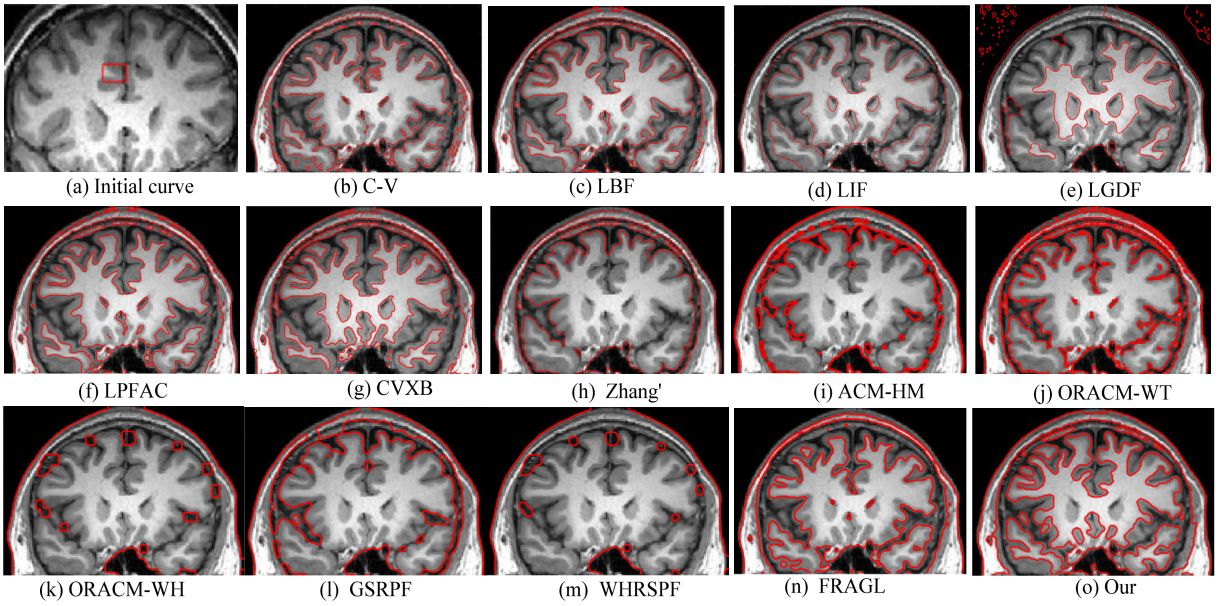

FIGURE 11. Segmentation results of the medical image using fourteen models. (a) The input image with Initial curve; (b) C-V; (c) LBF; (d) LIF; (e) LGDF; (f) LPFAC; (g) CVXB; (h) Zhang's; (i) ACM-HM; (j) ORACM-WT; (k) ORACM-WH; (l) GSRPF; (m) WHRSPF; (n) FRAGL; (o) our model.

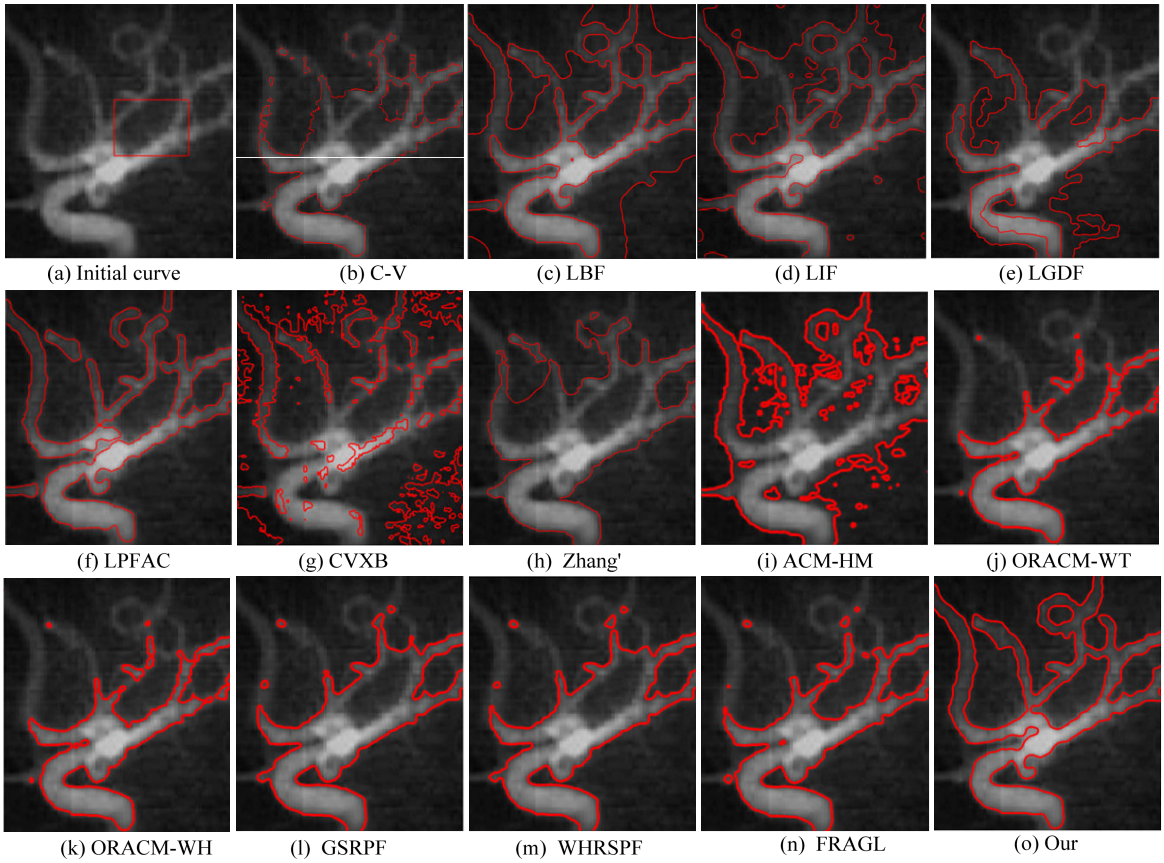

FIGURE 12. Segmentation results of the medical image using fourteen models. (a) The input image with Initial curve; (b) C-V; (c) LBF; (d) LIF; (e) LGDF; (f) LPFAC; (g) CVXB; (h) Zhang's; (i) ACM-HM; (j) ORACM-WT; (k) ORACM-WH; (l) GSRPF; (m) WHRSPF; (n) FRAGL; (o) our model.

In the LGDF model, the Gaussian noise cannot suppress the effect of the intensity InH. In the LPFAC model, the local pre-fitting energy cannot extract local image information during the curve evolution. In the CVXB model, the bias correction cannot coincide with the noise in the given segmented images. Thus, its segmentation results are not accurate. In the

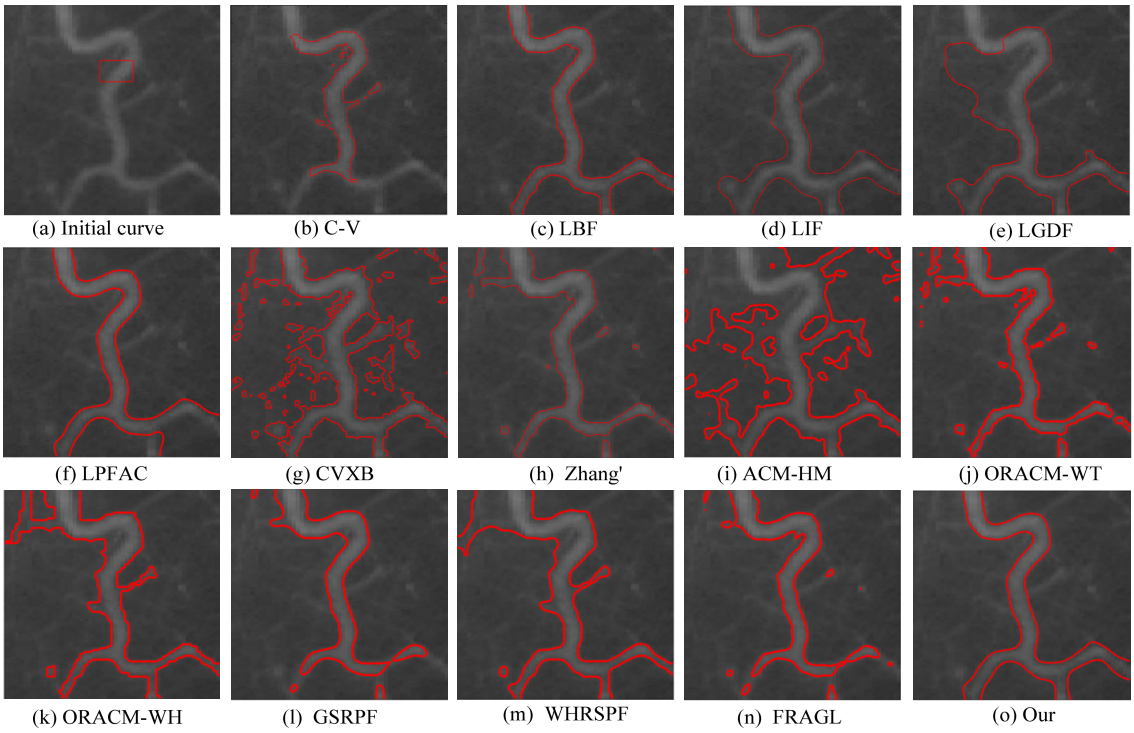

FIGURE 13. Segmentation results of the medical image using fourteen models. (a) The input image with Initial curve; (b) C-V; (c) LBF; (d) LIF; (e) LGDF; (f) LPFAC; (g) CVXB; (h) Zhang's; (i) ACM-HM; (j) ORACM-WT; (k) ORACM-WH; (l) GSRPF; (m) WHRSPF; (n) FRAGL; (o) our model.

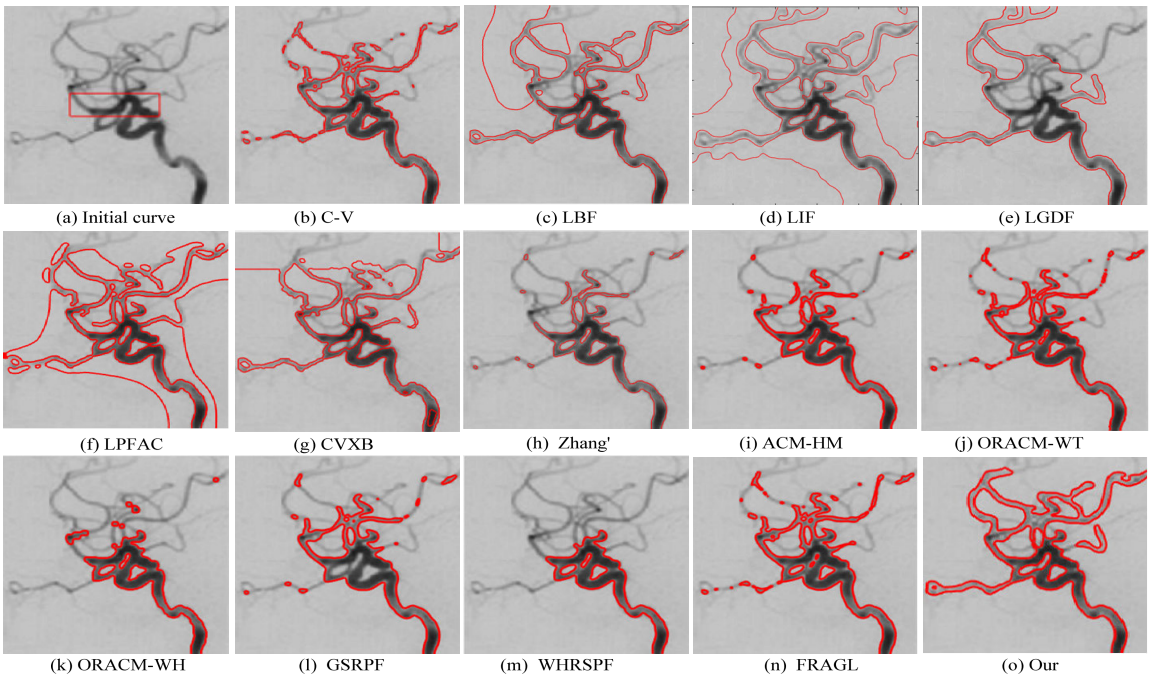

FIGURE 14. Segmentation results of the medical image using fourteen models. (a) The input image with Initial curve; (b) C-V; (c) LBF; (d) LIF; (e) LGDF; (f) LPFAC; (g) CVXB; (h) Zhang's; (i) ACM-HM; (j) ORACM-WT; (k) ORACM-WH; (l) GSRPF; (m) WHRSPF; (n) FRAGL; (o) our model.

Zhang's model, the global image information assumes that the object region is homogeneous, which causes many small object regions. Similar to the Zhang's model, the ORACM (ORACM-WT and ORACM-WH) models also compute the average intensity differences of two sides of the evolution curve as the driving force. Thus, two ORACM models neglect the slow change of the neighborhood points and also assumes that the object region is homogeneous. But, the ORACM-WT

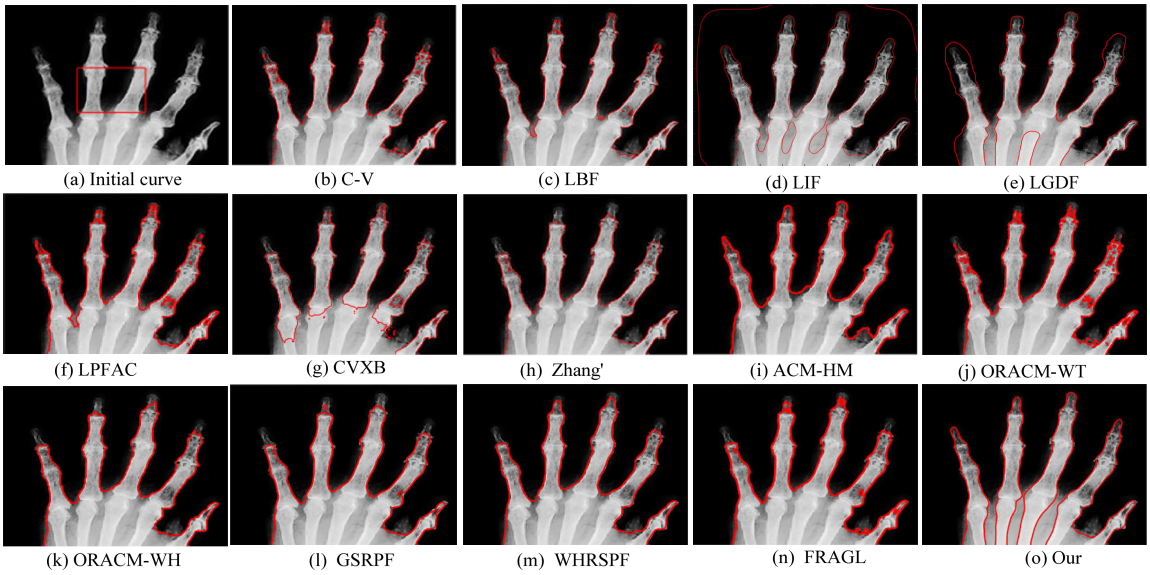

FIGURE 15. Segmentation results of the medical image using fourteen models. (a) The input image with Initial curve; (b) C-V; (c) LBF; (d) LIF; (e) LGDF; (f) LPFAC; (g) CVXB; (h) Zhang's; (i) ACM-HM; (j) ORACM-WT; (k) ORACM-WH; (l) GSRPF; (m) WHRSPF; (n) FRAGL; (o) our model.

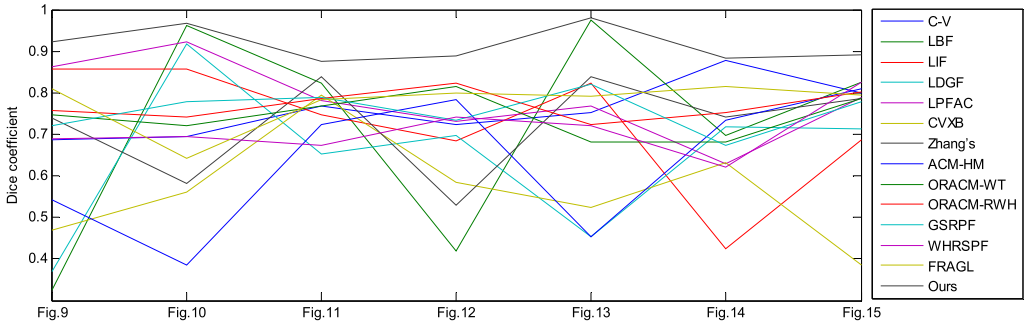

FIGURE 16. Comparison of the region-based ACMs in terms the Dice coefficient.

model causes smaller regions than the ORACM-WH model since the former with morphological operations can reduce the effect of noise. In the ACM-HM model, the derivative of the LSF in (9) is replaced by the eigenvalues of Hessian matrix, which can decrease the effect of noise. But the model can only extract the brightest regions due to its use of a second order derivative. Thus, the ACM-HM model can only extract the brightest regions. In the GSRPF model, the GSRPF as the driving force is formulated by incorporating local image characteristics, which is based on the local mean values of the inner and outer regions of the evolution curve instead of the global mean values, and can attain the satisfactory segmentation results for image with intensity InH. However, the GSRPF model is still not accurate enough to attain the desired object regions since the quadratic function with the median of the global intensity cannot control the propagation of the evolving curve. In the WHRSPF model, the global and local region-based SPF (GLRSPF) as the driving force consists of a weighted global region-based SPF (GRSPF) function and a weighted local region-based SPF (LRSPF) function, and an automatic force propagation function based on the image characteristics is introduced. However, the weights in the WHRSPF model needs to set manually. However, in our works, the GSEPF and the LSEPF are constructed by incorporating the global and local image information, respectively.

E. COMPUTATIONAL COMPLEXITY

In a given image, assuming the number of pixels is N, the size of the local window size is k. From (25), it is intuitive that the complexity of the GSEPF model and the LSEPF model are $O(N)$ and $O(k^2N)$, respectively. The proposed model is constructed by incorporating the GSEPF model and the LRSPF model. Therefore, the computational complexity of the proposed model $O((k^2+1)N) \approx O(N)$ since the local window.size k is very small. Similarly, the computational complexity of the Zhang's, ORACM-WH, ORACM-WT, and GSRPF models are all $O(N)$.

Table 1 shows the running time (in seconds) during iterations using fourteen models for segmenting the images corresponding to Fig. 9-15.It is intuitive that the LBF, LIF, and LDGF models take more running time than other models. And two ORACM models, the ACM-HM model, and the

TABLE 1. Comparison of the region-based ACMs in terms of running time(seconds).

Image	Fig. 9		Fig. 10		Fig. 11		Fig. 12		Fig. 13		Fig. 14		Fig. 15	
	Iteration/Time		Iteration/Time		Iteration/Time		Iteration/Time		Iteration/Time		Iteration/Time		Iteration/Time	
C-V	500	4.578	500	3.397	500	2.889	500	17.377	500	3.359	500	9.896	500	5.102
LBF	400	19.722	400	17.597	400	18.779	400	58.026	400	18.146	400	44.396	400	30.274
LIF	200	27.450	200	24.998	200	30.038	200	38.180	200	25.264	200	39.673	200	31.531
LDGF	2000	23.522	1000	19.420	2000	17.154	2000	71.889	2000	18.233	2000	43.286	2000	25.005
LPFAC	900	5.434	900	4.384	900	4.408	900	17.866	900	4.425	900	11.268	900	5.898
CVXB	200	1.634	200	1.119	200	0.614	200	4.347	200	0.939	200	2.488	200	1.028
Zhang's	120	6.219	120	5.686	120	7.898	260	42.317	70	3.014	120	11.437	120	6.716
ACM-HM	50	0.130	50	0.1146	50	0.107	50	0.280	50	0.117	50	0.215	50	0.140
ORACM-WT	4	0.2893	7	0.8131	5	0.2978	8	0.8529	7	0.4954	8	0.7248	5	0.466
ORACM-WH	7	0.3750	8	0.4096	2	0.2131	8	0.7485	2	0.1042	7	0.5582	2	0.297
GSRPF	100	0.889	100	0.702	100	0.639	100	2.433	100	0.811	100	1.872	100	0.967
WHRSPF	100	3.100	100	2.866	100	2.727	100	4.812	100	2.662	100	3.899	100	3.182
FRAGL	100	5.324	100	4.694	100	4.438	100	8.802	100	4.654	100	6.486	100	4.964
Ours	100	2.468	100	2.479	100	**2.541**	**100**	**3.072**	**100**	**2.395**	**100**	**2.867**	**100**	**2.411**

GSRPF model takes less running time than our model. From above analysis, our model has similar complexity to the 0Zhang's model and two ORACM models. Therefore, our model takes almost the same average running time compared with the popular ACMs.

V. CONCLUSION

A novel ACM guided by the global and local signed energy-based pressure force is proposed to segment images in the present of intensity InH and noise. Some important conclusions can be summarized as follows.

(1) A global data term with global image information is designed, which is driven by the GSEPF. The GSEPF is formulated by computing the energy difference between the inner and outer energies of the evolution curve, and can effectively segment the homogeneious images.

(2) A local data term with local image information is proposed, which is driven by the LSEPF. The LSEPF is constructed by computing the pixel-by-pixel energy difference within the local neighborhood region, which can accurately extract the desired objects from the inhomogeneious images.

(3) According to the image characteristics, the global and local variances are used to balance the weight of the GSEPF and the LSEPF, which can solve the problem of setting parameters. In addition, a regularization term and a penalty term are added to avoid the re-initialization process and smooth the LSF.

(4) By incorporating the global and local image information, the proposed model can accurately detect the desired objects from images with intensity InH and noise. Furthermore, the proposed model has higher accuracy in terms of the average Dice coefficient compared with thirteenth ACMs.

(5) It is noticed that the proposed model is mainly applied to two-phase image segmentation. In the future, an effective multi-phase image segmentation method to deal with intensity InH will be developed. In addition, the proposed model poorly segments the color images [38] since it only utilizes the intensity information. Therefore, another extension of this work is to study the color image segmentation.

REFERENCES

[1] E. Karami, M. S. Shehata, and A. Smith, "Adaptive polar active contour for segmentation and tracking in ultrasound videos," *IEEE Trans. Circuits Syst. Video Technol.*, vol. 29, no. 4, pp. 1209–1222, Apr. 2019.

[2] C. Cuenca, E. González, A. Trujillo, J. Esclarín, L. Mazorra, L. Alvarez, J. A. Martínez-Mera, P. G. Tahoces, and J. M. Carreira, "Ellipse motion estimation using parametric snakes," *J. Real-Time Image Process.*, vol. 14, no. 4, pp. 793–802, 2018.

[3] M. Kass, A. Witkin, and D. Terzopoulos, "Snakes: Active contour models," *Int. J. Comput. Vis.*, vol. 1, no. 4, pp. 321–331, Jan. 1988.

[4] S. C. Zhu and A. Yuille, "Region competition: Unifying snakes, region growing, and Bayes/MDL for multiband image segmentation," *IEEE Trans. Pattern Anal. Mach. Intell.*, vol. 18, no. 9, pp. 884–900, Sep. 1996.

[5] V. Caselles, R. Kimmel, and G. Sapiro, "Geodesic active contours," *Int. J. Comput. Vis.*, vol. 22, no. 1, pp. 61–79, 1997.

[6] T. F. Chan and L. A. Vese, "Active contours without edges," *IEEE Trans. Image Process.*, vol. 10, no. 2, pp. 266–277, Feb. 2001.

[7] L. Vese and T. Chan, "A multiphase level set framework for image segmentation using the Mumford and Shah model," *Int. J. Comput. Vis.*, vol. 50, no. 3, pp. 271–293, 2002.

[8] D. Mumford and J. Shah, "Optimal approximations by piecewise smooth functions and associated variational problems," *Commun. Pure Appl. Math.*, vol. 42, no. 5, pp. 577–685, 1989.

[9] S. Krinidis and V. Chatzis, "Fuzzy energy-based active contours," *IEEE Trans. Image Process.*, vol. 18, no. 12, pp. 2747–2755, Dec. 2009.

[10] J. Fang, H. Liu, H. Liu, L. Zhang, J. Liu, H. Zhang, and C. Liu, "Multiresolution convex variational model for multiphase image segmentation," *Comput. Electr. Eng.*, vol. 54, pp. 230–245, Aug. 2016.

[11] L. Sun, X. Meng, J. Xu, and S. Zhang, "An image segmentation method based on improved regularized level set model," *Appl. Sci.*, vol. 8, no. 12, 2018, Art. no. 2393.

[12] J. Fang, H. Liu, L. Zhang, J. Liu, and H. Liu, "Fuzzy region-based active contours driven by weighting global and local fitting energy," *IEEE Access*, vol. 7, pp. 184518–184536, 2019.

[13] B. N. Li, C. K. Chui, S. H. Ong, T. Numano, T. Washio, K. Homma, S. Chang, S. Venkatesh, E. Kobayashi, "Modeling shear modulus distribution in magnetic resonance elastography with piecewise constant level sets," *Magn. Reson. Imag.*, vol. 30, no. 3, pp. 390–401, 2012.

[14] C. Li, C.-Y. Kao, J. C. Gore, and Z. Ding, "Minimization of region-scalable fitting energy for image segmentation," *IEEE Trans. Image Process.*, vol. 17, no. 10, pp. 1940–1949, Oct. 2008.

[15] C. Li, C.-Y. Kao, J. C. Gore, and Z. Ding, "Implicit active contours driven by local binary fitting energy," in *Proc. IEEE Conf. Comput. Vis. Pattern Recognit.*, Jun. 2007, pp. 1–7.

[16] K. Zhang, H. Song, and L. Zhang, "Active contours driven by local image fitting energy," *Pattern Recognit.*, vol. 43, no. 4, pp. 1199–1206, Apr. 2010.

[17] Z. Ji, Y. Xia, Q. Sun, G. Cao, and Q. Chen, "Active contours driven by local likelihood image fitting energy for image segmentation," *Inf. Sci.*, vol. 301, pp. 285–304, Apr. 2015.

[18] L. Wang, Y. Chang, H. Wang, Z. Wu, J. Pu, and X. Yang, "An active contour model based on local fitted images for image segmentation," *Inf. Sci.*, vols. 418–419, pp. 61–73, Dec. 2017.

[19] L. Wang, L. He, A. Mishra, and C. Li, "Active contours driven by local Gaussian distribution fitting energy," *Signal Process.*, vol. 89, no. 12, pp. 2435–2447, Dec. 2009.
[20] C. He, Y. Wang, and Q. Chen, "Active contours driven by weighted region-scalable fitting energy based on local entropy," *Signal Process.*, vol. 92, no. 2, pp. 587–600, Feb. 2012.
[21] J. Miao, T.-Z. Huang, X. Zhou, Y. Wang, and J. Liu, "Image segmentation based on an active contour model of partial image restoration with local cosine fitting energy," *Inf. Sci.*, vol. 447, pp. 52–71, Jun. 2018.
[22] K. Ding, L. Xiao, and G. Weng, "Active contours driven by local pre-fitting energy for fast image segmentation," *Pattern Recognit. Lett.*, vol. 104, pp. 29–36, Mar. 2018.
[23] L. Fang, T. Qiu, H. Zhao, and F. Lv, "A hybrid active contour model based on global and local information for medical image segmentation," *Multidimensional Syst. Signal Process.*, vol. 30, no. 2, pp. 689–703, Apr. 2019.
[24] D. Zosso, J. An, J. Stevick, N. Takaki, M. Weiss, L. S. Slaughter, H. H. Cao, P. S. Weiss, and A. L. Bertozzi, "Image segmentation with dynamic artifacts detection and bias correction," *Inverse Problems Imag.*, vol. 11, no. 3, pp. 577–600, 2017.
[25] B. Dong, R. Jin, and G. Weng, "Active contour model based on local bias field estimation for image segmentation," *Signal Process., Image Commun.*, vol. 78, pp. 187–199, Oct. 2019.
[26] H. Yu, F. He, and Y. Pan, "A novel region-based active contour model via local patch similarity measure for image segmentation," *Multimedia Tools Appl.*, vol. 77, no. 18, pp. 24097–24119, Sep. 2018.
[27] L. Chen, Y. Zhou, Y. Wang, and J. Yang, "GACV: Geodesic-Aided CV method," *Pattern Recognit.*, vol. 39, no. 7, pp. 1391–1395, 2006.
[28] H. Ali, N. Badshah, K. Chen, and G. A. Khan, "A variational model with hybrid images data fitting energies for segmentation of images with intensity inhomogeneity," *Pattern Recognit.*, vol. 51, pp. 27–42, Mar. 2016.
[29] C. Li, C. Xu, C. Gui, and M. D. Fox, "Distance regularized level set evolution and its application to image segmentation," *IEEE Trans. Image Process.*, vol. 19, no. 12, pp. 3243–3254, Dec. 2010.
[30] K. Zhang, L. Zhang, H. Song, and W. Zhou, "Active contours with selective local or global segmentation: A new formulation and level set method," *Image Vis. Comput.*, vol. 28, no. 4, pp. 668–676, Apr. 2010.
[31] M. F. Talu, "ORACM: Online region-based active contour model," *Expert Syst. Appl.*, vol. 40, no. 16, pp. 6233–6240, Nov. 2013.
[32] K. Hanbay and M. F. Talu, "A novel active contour model for medical images via the hessian matrix and eigenvalues," *Comput. Math. Appl.*, vol. 75, no. 9, pp. 3081–3104, May 2018.
[33] M. M. Abdelsamea and S. A. Tsaftaris, "Active contour model driven by globally signed region pressure force," in *Proc. 18th Int. Conf. Digit. Signal Process. (DSP)*, Fira, Greece, Jul. 2013, pp. 430–436.
[34] A. Azizi and K. Elkourd, "Fast region-based active contour model driven by local signed pressure force," *ELCVIA, Electron. Lett. Comput. Vis. Image Anal.*, vol. 15, no. 1, pp. 1–13, 2016.
[35] L. Sun, X. Meng, J. Xu, and Y. Tian, "An image segmentation method using an active contour model based on improved SPF and LIF," *Appl. Sci.*, vol. 8, no. 12, p. 2576, 2018.
[36] B. Han and Y. Wu, "Active contours driven by global and local weighted signed pressure force for image segmentation," *Pattern Recognit.*, vol. 88, pp. 715–728, Apr. 2019.
[37] J. Fang, H. Liu, L. Zhang, J. Liu, and H. Liu, "Active contour driven by weighted hybrid signed pressure force for image segmentation," *IEEE Access*, vol. 7, pp. 97492–97504, 2019.
[38] D. Martin, C. Fowlkes, D. Tal, and J. Malik, "A database of human segmented natural images and its application to evaluating segmentation algorithms and measuring ecological statistics," in *Proc. 8th IEEE Int. Conf. Comput. Vis. (ICCV)*, Vancouver, BC, Canada, Nov. 2002, pp. 416–423.

HUAXIANG LIU received the B.S. and M.S. degrees in circuits and systems from Hunan Normal University, in 2007 and 2010, respectively. She is currently pursuing the Ph.D. degree with Central South University. She is also a teacher with the East China University of Technology. Her research interests include medical image segmentation, deep learning, and machine learning.

JIANGXIONG FANG received the B.S. and M.S. degrees from Central South University, Changsha, China, in 2004 and 2007, respectively, and the Ph.D. degree in pattern recognition and intelligent system from the Institute of Image Processing and Pattern Recognition, Shanghai Jiao Tong University, Shanghai, China, in 2012. He is currently an Associate Professor with the East China University of Technology. His research interests include image segmentation and deep learning.

ZIJIAN ZHANG received the B.S. degree in nuclear engineering and nuclear technology from the University of South China, in 2009. He is currently pursuing the master's degree with the School of Physics and Electronics, Shandong Normal University. He is also a Superior Medical Physicist with the Xiangya Hospital, Central South University. His research interests include radiomics and the use of artificial intelligence in the area of radiotherapy.

YONGCHENG LIN received the B.S. and M.S. degrees from Liaoning Shihua University, Fushun, China, in 2000 and 2003, respectively, and the Ph.D. degree from Tianjin University, Tianjin, China, in 2006. He is currently a Full Professor with the College of Mechanical and Electrical Engineering, Central South University. His major research interests include intelligent manufacturing technology and intelligent equipment, material forming control technology, and image processing. He got the support of the Yangtze River Scholars Award Plan, China, in 2015.